Automating Perturbation Experiments for a Hopping Robot using a Cable-Driven Impedance Haptic Device

SeungHoon Han

A thesis

submitted in partial fulfillment of the

requirements for the degree of

Master of Science in Mechanical Engineering

University of Washington

2018

Committee:

Samuel A. Burden, Chair

Santosh Devasia

Sawyer B. Fuller

Program Authorized to Offer Degree:

Mechanical Engineering

University of Washington

Abstract

Automating Perturbation Experiments for a Hopping Robot using
a Cable-Driven Impedance Haptic Device

SeungHoon Han

Chair of the Supervisory Committee:
Assistant Professor Samuel A. Burden
Department of Electrical Engineering

DARPA Robotics Challenge revealed a need for testing/perturbing robots in systematic methods and testing robots in different environments. The goal of this research is to design a testbed that can render virtual dynamics to emulate different environments on a robot and perturb it in a systematic method. A novel perspective of a haptic system is proposed in which a robot is considered as the “user” and the testbed motors are considered as the “haptic device”. Similar to a generic haptic device, the testbed motors will render forces that would be present if the robot were directly interacting with a virtual environment. A cable-driven testbed for a 1 DOF jumping robot (hopper) is introduced and a model-based force control is used to control the haptic device. Next, the performance of the haptic device is characterized by using a sum of sines trajectory with FFT algorithm. The result yields that the haptic system will apply 13N of force error to the hopper. Finally, the testbed is tested with the hopper in the loop by performing two tests: haptic devices applying a zero net force and applying a positive net force.

TABLE OF CONTENTS

Page

List of Figures

Figure Number Page

Acknowledgment

I would like to express my sincere gratitude to Sam Burden and Tom Libby. Sam Burden, an EE assistant professor, graciously took me in as his MS student and provided all the resources for the research as well as guidance. Tom Libby, a postdoc from University of California, Berkeley, co-advised my research and gave insightful perspective as well as mentorship. With the guidance from Sam and Tom, I enjoyed my research and gained a lot of knowledge in the field of robotics. I also want to thank Andrew Pace, an EE Ph.D. student, who helped me out throughout my thesis and Tianqi Li, a ME MS student, who also worked on the jumping robot. Furthermore, I want to thank the Bio Robotics Lab community and all the lab mates who were part of my journey. Last, I want to thank my family for always being supportive.

Chapter 1

Introduction

This chapter addresses the state of the art methods of robot testing and discloses the motivation and goal for the research. Furthermore, it introduces a novel perspective of interpreting a conventional haptic system.

1.1 Motivation

Despite the state of the art of robotics, DARPA (Defense Advanced Research Projects Agency) Robotics Challenge revealed that the emphasis on testing robots has been undermined. There are two major problems when testing robots.

First, many of the robots' gait/stance stability is tested in an inadequate method such as pushing, shoving, and kicking. However, these are not scientific methods to quantify the perturbation on the robot. Therefore, a testbed that can accurately quantify the perturbation will not only yield the robot's robustness, but also give researchers a better understanding of the performance of the robot.

Second, many of the robots do not perform well in the real world compared to that of the laboratories. The end goal of any robots is to deploy it into the real world and have the confidence that it will perform as expected. This requires testing robots in the real world which can be expensive and risky. Therefore, designing a systematic testbed inside a lab that can simulate different environments for the robot can mitigate any unpredictable risks.

This testbed will not only assist analyzing the dynamics of the robots under perturbation but also render different environments for the robots. In short, the goal of this research is to design a testbed that can render virtual dynamics to emulate different environments on a robot and perturb it in a systematic/repeatable method.

1.2 Cable - Driven Testbed for Jumping Robot

The robot used for this research is a four-legged robot (Minitaur) from Ghost Robotics as shown in Figure 1.1. This robot can trot as well as jump. The overarching goal is to design a testbed for the Minitaur in which the testbed can perturb the robot in multi DOF at any instantaneous time and have minimal influence in robot dynamics when applying no perturbation. When applying perturbation on the robot, the robot dynamics will change as well as the “environment” that the robot will be operating.

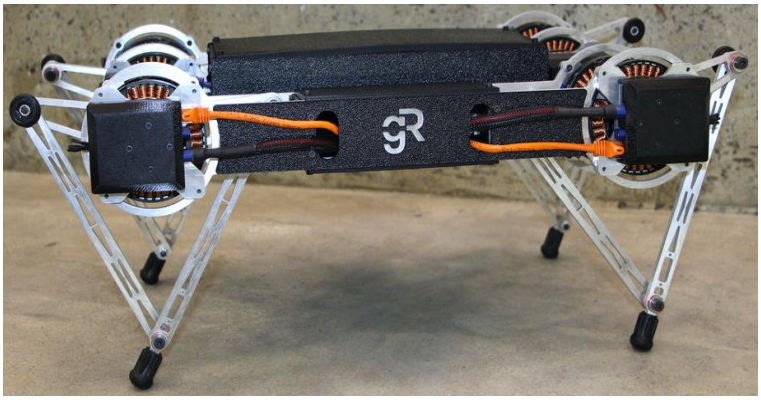

Figure 1.1. Four-legged Minitaur robot from Ghost Robotics

There are many ways to build an automated testbed. Georgia Tech's SCATTER (Systematic Creation of Arbitrary Terrain and Testing of Exploratory Robots) systematically controls the initial condition of the terrain to understand the robot locomotion on heterogeneous substrates [4]. The testbed uses air fluidized bed and tilting actuator to automatically alter the mesh system for the robot.

From various methods of perturbing the robot such as using a linear actuator or pneumatic actuator, the cable mechanism was chosen. The inspiration for the choice of cable mechanism originated from the parallel robot design as shown in Figure 1.2 [3]. Cable-driven parallel robots use motors, pulleys, and cables as the source of actuation. One end of the cable is attached to a motor and the other end is attached to the object. The number of cables, motors, and pulleys can vary depending on the design. Besides the advantage of workspace, the cable design is much lighter [2] compared to other mechanisms such as linear actuator and pneumatic actuator.

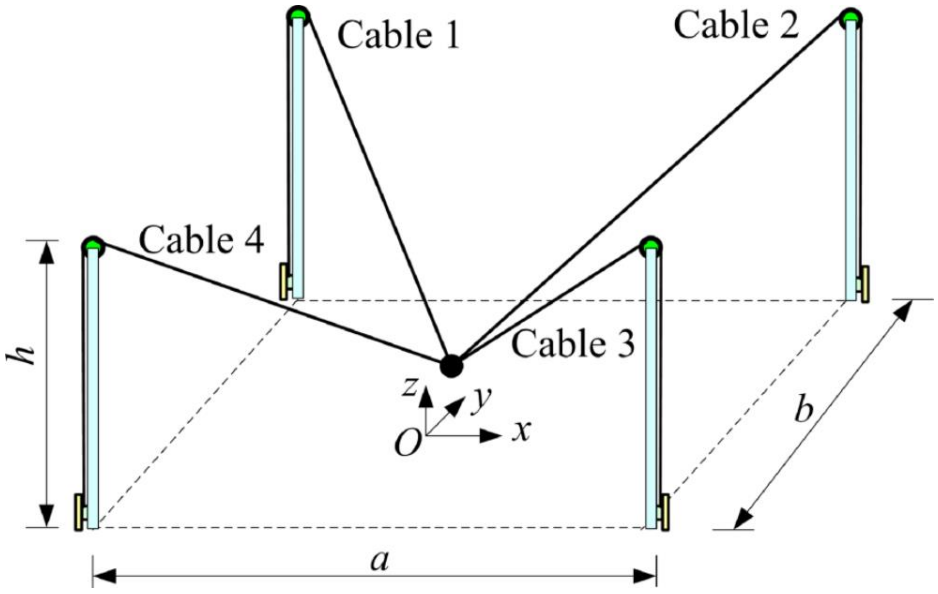

Figure 1.2. A schematic diagram of a conventional cable-driven parallel robot in which the object ('O') is static.

Unlike most of the traditional parallel robots where the object is static, this testbed will have the Minitaur robot as the object. This is a unique approach because the object is contact rich with rapid change in dynamics. Figure 1.3 illustrates the simple diagram of the Minitaur that's connected to cables. There will be even number of motor and cable pairs to keep the tension. Furthermore, motion capturing camera will be placed around the testbed to monitor the robot's dynamics. Compared to the static objects which does not have physical impact, this approach will have impact which can cause slack in the cable. So, the challenge will be keeping the cable from going slack.

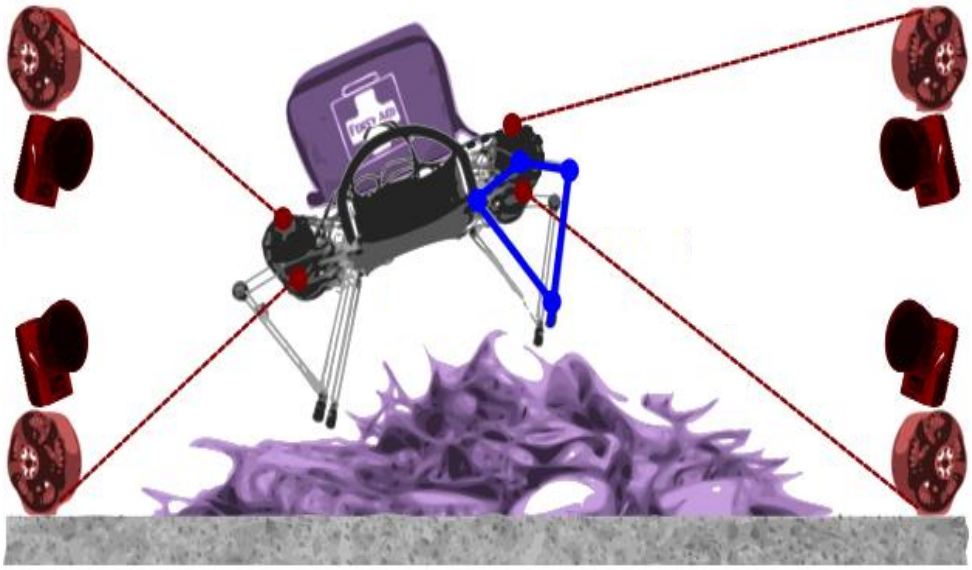

Figure 1.3. Cable-driven parallel robot with the Minitaur robot as the object. One of the legs (highlighted blue) will be used for testing

To test this concept of the testbed, this research focused on designing a 1 DOF testbed for one of the legs of the Minitaur (hopper) as shown in Figure 1.4 (A). The motion capturing camera is placed 2m from the testbed to capture the hopper's height. The testbed should have design requirements as listed below.

1. Apply forces over the range of frequencies the hopper resides
2. Provide force up to 10 times the weight of the robot
3. Provide velocity up to 5 times the linear velocity of the robot

Furthermore, the testbed should be able to perform the following two tasks.

1. When the two external motors apply a zero net force with the cables attached to the robot, the hopper dynamics should be close to the hopper jumping without the cable attachment. In other words, the testbed should have minimal influence in robot dynamics when applying zero net force perturbation.
2. When the two external motors apply a positive net force with the cables attached to the robot, the hopper will be perturbed with an upward force in which it will experience less gravity. The hopper should jump higher at a lower frequency as if it is jumping on the moon.

This testbed's application is similar to a haptics system because the top/bottom motors of the testbed need to render forces on the hopper which will change the environment that the hopper resides.

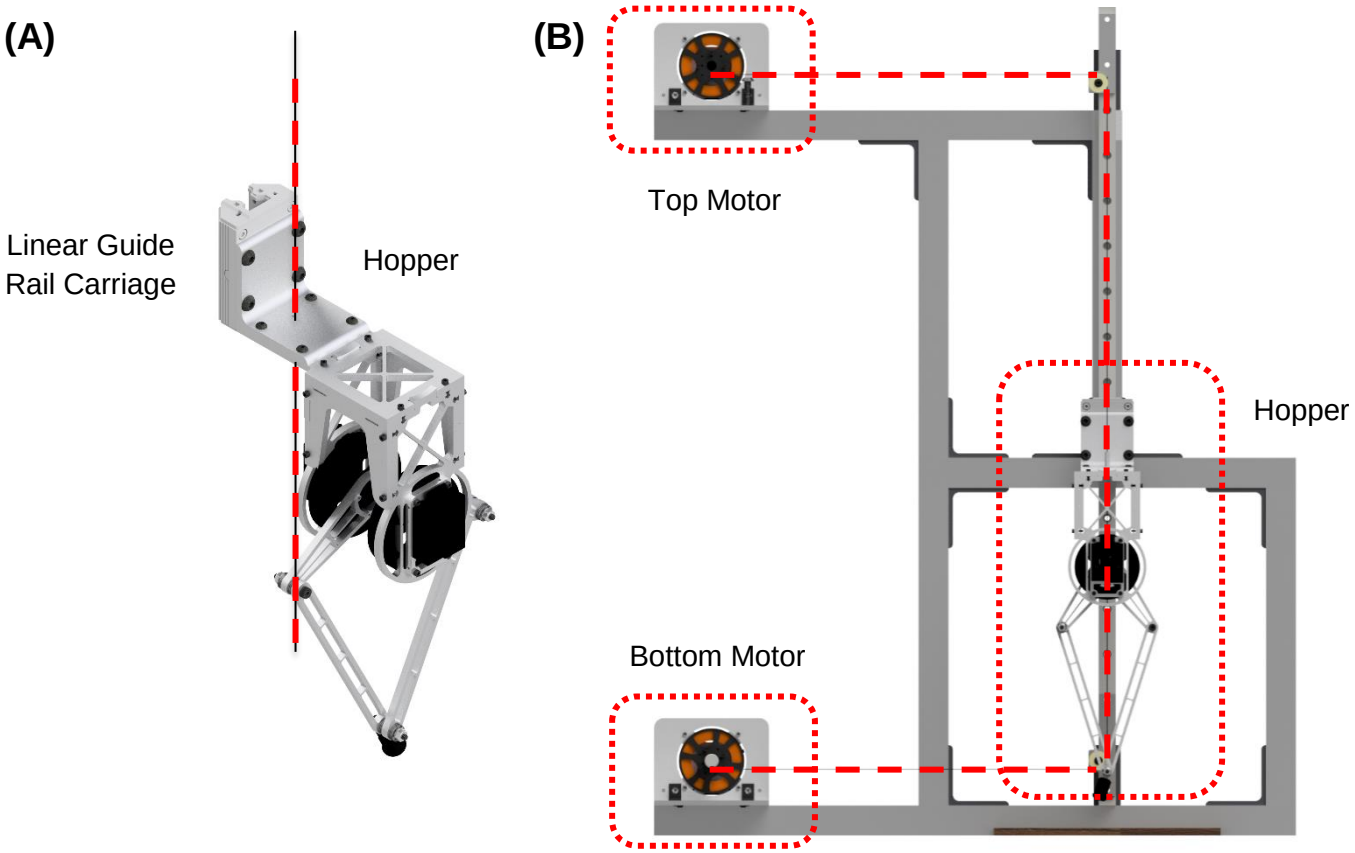

Figure 1.4. One of the legs of the Minitaur (hopper), constrained to 1DOF via a linear guide rail. Top cable is attached to the top plate of the hopper and the bottom cable is attached to the bottom plate of the hopper. (Not one cable) (A) Each of the cables are attached to two separate motors. Light nylon pulleys are used to redirect the force. More in depth of the mechanical design of the testbed will be mentioned in Chapter 2.

1.3 Introduction to Haptics and Haptic Loop

If the robot is interacting with the testbed that's applying a constant upward force to the robot, it experiences a less gravity virtual environment. This is similar to a human interacting with the haptic device and experiencing virtual environment.

In fact, the definition of haptics can be generalized as "In the robotics and virtual reality literature, haptics is broadly defined as real and simulated touch interactions between robots, humans, and real, remote, or simulated environments, in various combinations" [1].

In this alternative perspective of haptics, a robot can be considered as the "user" and the two-external top/bottom motors of the testbed as the "haptic device". Similar to a generic haptic device, the two-external top/bottom motors (haptic device) will render forces that would be present if the robot (user) were interacting directly with a virtual environment [2]. Therefore, if the two-external top/bottom motors apply forces on the hopper in which the hopper experiences a different environment, "virtual environment", this system can be considered as haptics.

The conventional haptic loop for a generic haptic interface as well as the haptic loop for the testbed is shown in Figure 1.5. Although the haptic interface for the testbed is different to traditional haptic interface involving a haptic device such as a phantom haptic device, the haptic loop can be implemented for the testbed. Once again, the two external motors are considered as the haptic device and the user is considered as the robot. As the hopper hops (constrained to 1DOF), the two haptic devices will sense the robot's velocity. ①. Then the sensed velocity will be sent to the mainboard ②. The mainboard will calculate the response of the environment that needs to be relayed back to the robot ③. Finally, the motors of the haptic device will provide the force to the robot ④. The haptic devices will provide forces such that the robot/user feels like it is interacting directly with a virtual environment. For example, if the haptic device renders a positive net force on the robot, the hopper should feel like it is jumping on a moon.

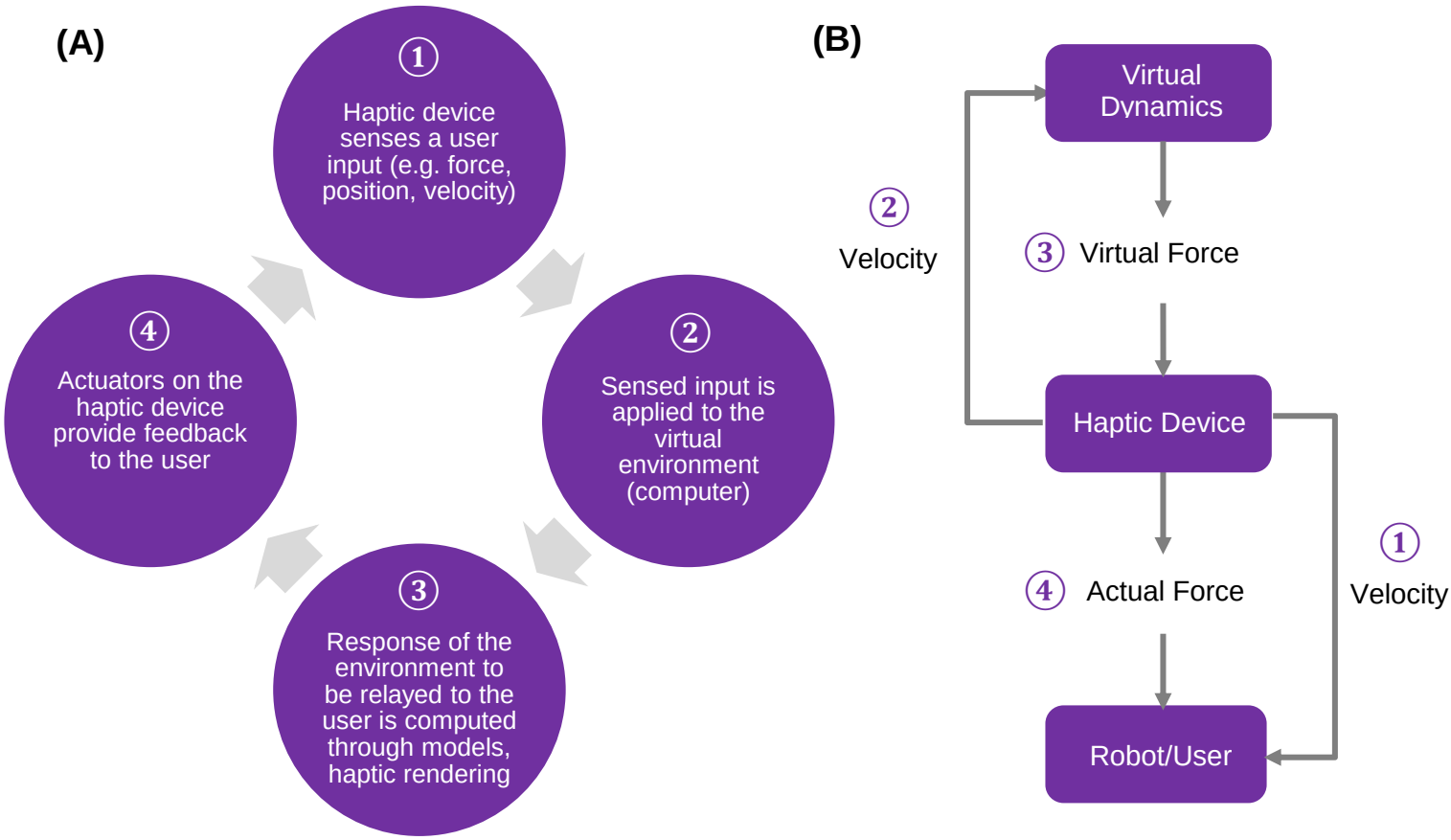

Figure 1.5. Haptic loop for a generic haptic interface (A). Haptic loop for the testbed (B)

1.4 Impedance Haptic Device & Requirements

There are two types of haptic devices: impedance and admittance devices [5]. Impedance haptic device senses the user's position/velocity and applies a force to back to the user. On the other hand, admittance haptic device senses the force applied by the user and constrains the user's position. Impedance type is force-controlled and have back-drivable motors with low inertia and friction in the system. Admittance type is velocity-controlled and are non-back-drivable with high-bandwidth low-level controller [1].

Since the motors used for the testbed are back drivable, the haptic device is closer to an impedance type. This method is also favorable because the admittance haptic device will require a high bandwidth motors and a load cell attached to the robot. The load cell reading (force) will be the input for the admittance type whereas velocity will be the input for the impedance type. Attaching a load cell to a system that is rich in contact can easily break a load cell.

There are couple requirements for an impedance type. First, the back drivable motors have to be a force source and provide high torque. Second, the system needs to have low friction and inertia. Last, the haptic device needs to measure the input (velocity) and apply the output (force) at a high rate (1k Hz) to ensure smooth, continuous movement. Since impedance haptic device has a position/velocity input with force output, the BLDC motors need to be able to perform force control which will be mentioned in Chapter 3.

Chapter 2

Mechanical Design of the Testbed

This chapter focuses on the mechanical design of the unique cable-driven haptic testbed. The haptic device was added onto the original testbed which was built by Yana Sosnovskaya [7] and Jake Baldassini [6] and minor modifications were made. The hopper uses voltage control and PD control to jump. Moreover, since the motors are back drivable, the configuration of the leg and set position of the motor influences the height in which the robot can jump as well as landing [10].

2.1 3D CAD Testbed

As shown in Figure 2.1, two identical haptic devices are located perpendicular to the robot and the plates of the haptic devices are designed to be adjustable in position. Cable driven mechanism provides increased motion range and is used in many robotics researches such as the Utah-MIT Dexterous Hand [8]. However, a challenge when using the cable is keeping the tension since cables cannot provide compressive force. A cable is attached to the top plate of the hopper and the other end is fastened to the top pulley. This is identical for the bottom motor. With

tension, the hopper with the haptic device will be considered as one rigid system. By applying opposite forces to the robot, the net force on the robot will be the key in manipulating gravity.

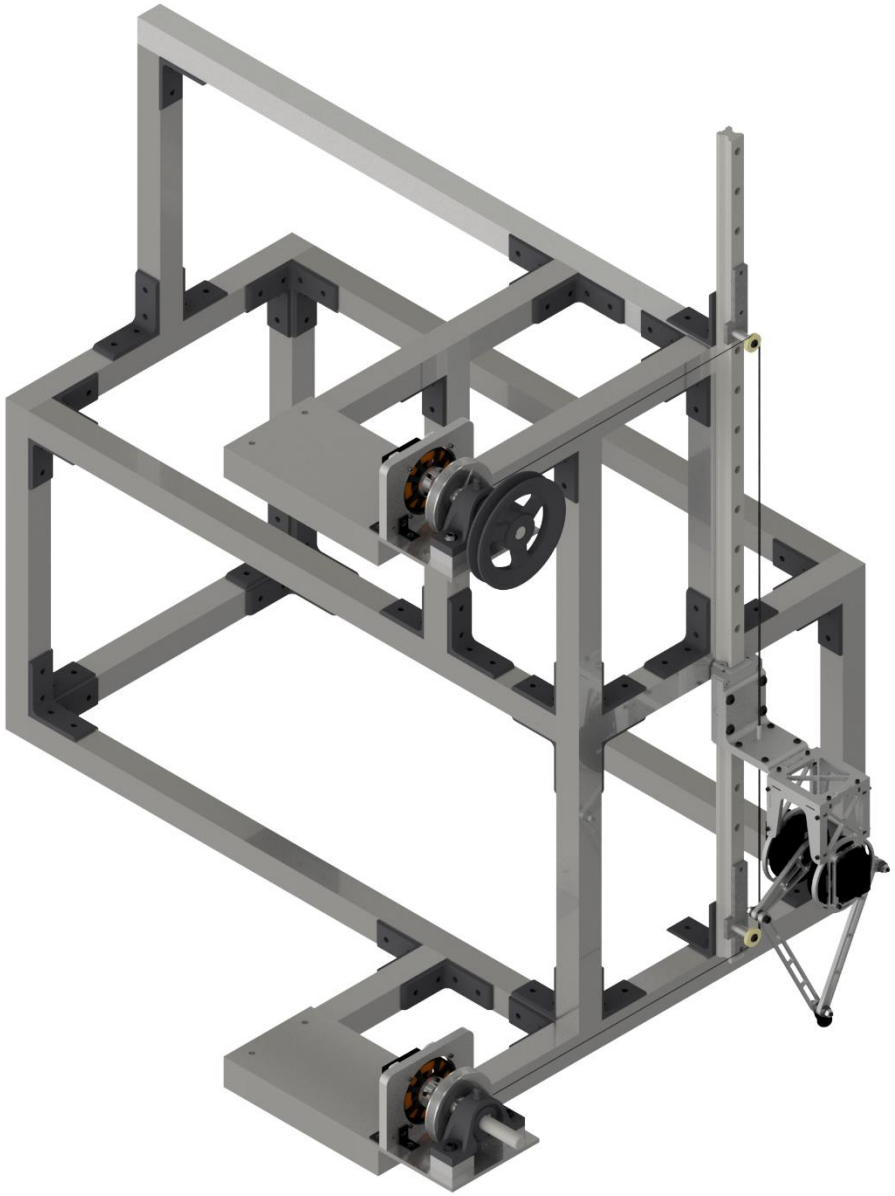

Figure 2.1. Full testbed modeled on Autodesk Inventor

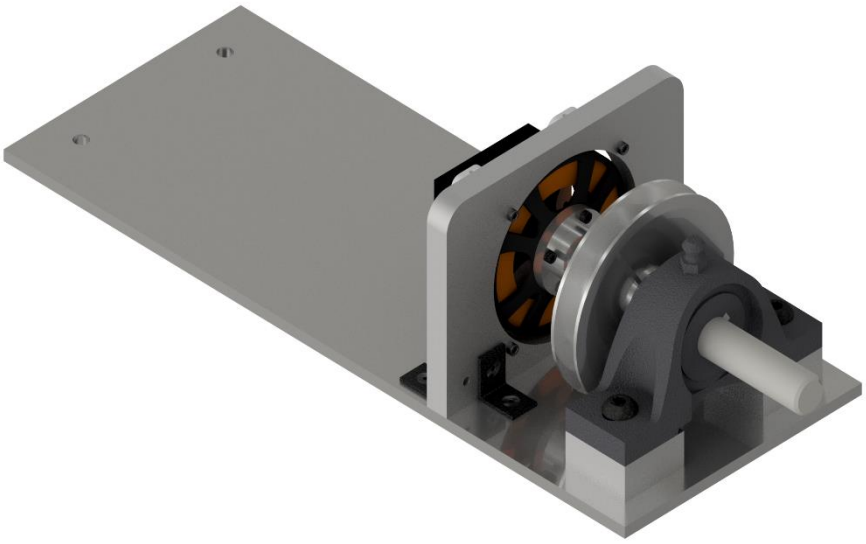

Figure 2.2. Haptic device modeled on Autodesk Inventor

2.2 Prototyping and Fabricating

Most of the parts are purchased from McMaster-Cart and 80/20 Inc. Before using the mill, lathe, and other hand tools at the ME workshop to fabricate the parts with aluminum, all the modules were prototyped using acrylic and laser cutter at the UW CoMotion MakerSpace. Modeling the testbed before fabricating minimized any potential hardware integration issues as well as mitigating cable misalignment. After confirming all the dimensions using parts made from acrylic, the parts were fabricated out of aluminum using mainly the lathe and the mill. The top plate of the hopper was designed but fabricated using a water jet. It is vital that the shaft is collinear to the motor's center of axis. Since a pulley as well as a flywheel (connected to increase moment of inertia to monitor the acceleration) are attached to the shaft, a slight misalignment about the axis can cause a moment, hence vibration in the system. The flywheel is only used for data collecting in Chapter 3. Images of the testbed can be found in the Appendix.

2.3. Pulley Size Selection

The same U8 Tiger motors that are on the hopper are used for the two haptic devices because an impedance haptic device require BLDC motors. Using the same motors on the mainboard also allows easier integration as well as keeping the motor update rate consistent (1k Hz). The motor constants, Kt and Kv, are 0.095 Nm/A and 100 RPM/V respectively with a motor resistance of 0.095 ohm. The stall torque and no-load speed can be calculated as shown below.

$$Stall\ Torque: K_t * \frac{V}{R} = 0.095\ \frac{Nm}{A} * \frac{16\ V}{0.186\ \Omega} = 8.172\ Nm \qquad \text{Eq 2.1}$$

$$No - load\ Speed: K_v * V = \ 100\ \frac{RPM}{V} * 16\ V = \ 1600\ RPM \qquad \text{Eq 2.2}$$

With the calculated stall torque and no-load speed, a torque speed curve of the motor can be plotted as shown below.

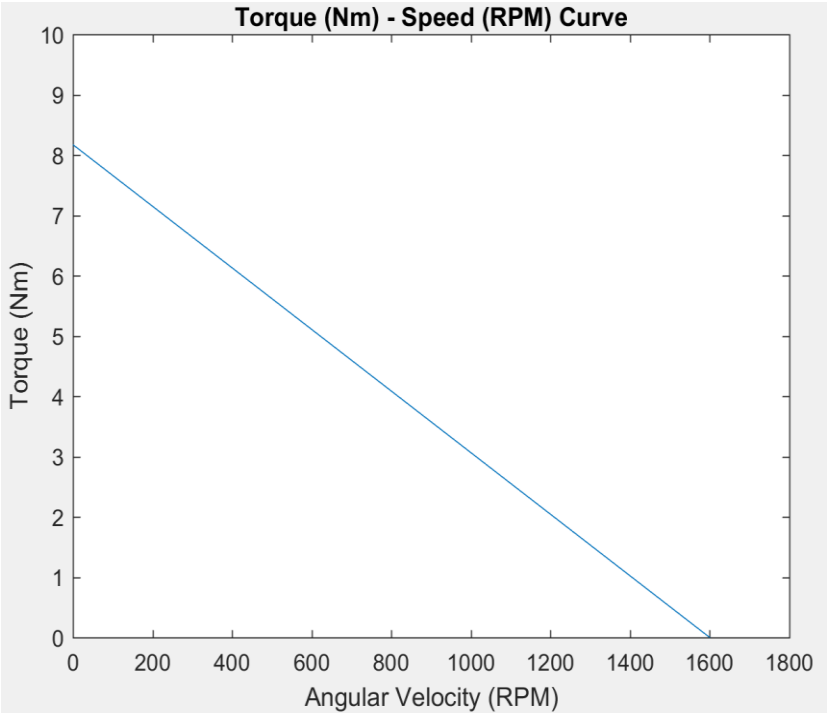

Figure 2.3. Calculated Torque (Nm) – Speed (RPM) Curve of the U8 motor

Since the pulley is attached to the motor, the size of the radius of a pulley can alter the magnitude of the output of linear force and velocity from the motor. A careful selection of pulley size is needed for the force and speed tradeoff of the motor. Force is inversely proportional to radius ($F = \tau/r$) whereas linear velocity is proportional to the radius ($v = r * \omega$). For a given torque and angular velocity, increasing the radius will decrease the force but increase the linear velocity. However, increasing the radius also increases the moment of inertia.

The hopper weighs 2.2Kg and its max speed is estimated to be around 1-2 m/s. This means that the motor should render minimum of force above 22 N and linear velocity of 1-2 m/s. With a radius of 0.0343 m the motor can render up to 238.32 N and a linear velocity of 5.75 m/s as shown below. Therefore, the motor will be able to apply up to 10 times the hopper weight and 5 times the speed of the hopper which is mentioned as the design requirements in Chapter 1.

$$F = \frac{Stall\ Torque}{r} = \frac{8.172\ Nm}{0.0343\ m} = 238.32\ N \quad \text{Eq 2.3}$$

$$v = Noload\ Speed * r = 1600RPM * \frac{0.104719755\ \frac{rad}{s}}{1\ RPM} * 0.0343\ m = 5.75\ \frac{m}{s} \quad \text{Eq 2.4}$$

The figure below shows that increasing the radius will decrease the force but increase the linear velocity. Radius of 0.05 m is chosen to exhibit the mechanical advantage when altering the radius of the pulley.

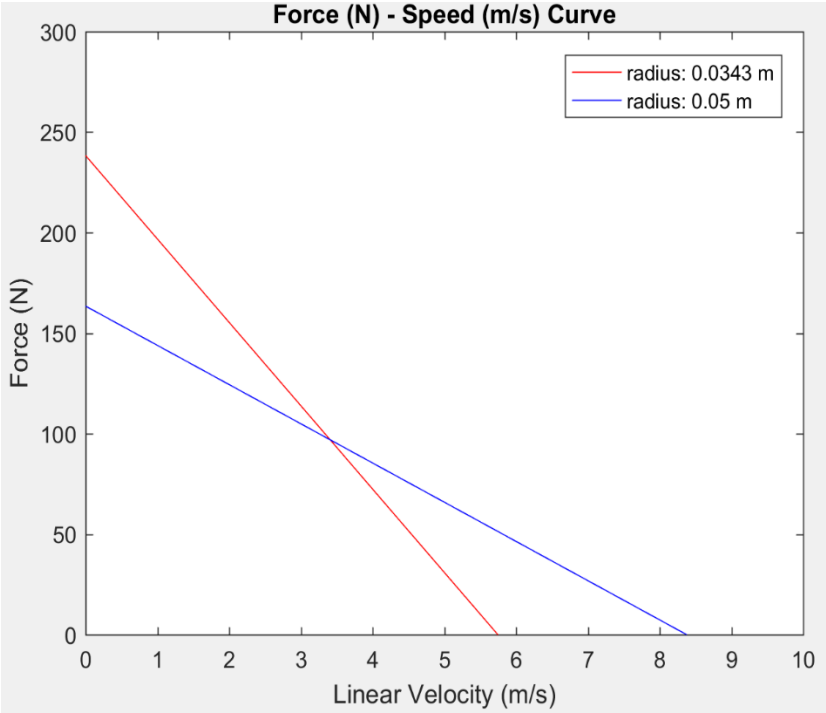

Figure 2.4. Calculated Force (N) – Linear Velocity (m/s)

.

Chapter 3

Model - Based Force Control

This chapter focuses on the method of implementing force control on a BLDC motor. As well as integrating a load cell into the mainboard to calibrate acceleration to force.

3.1 Back Electromotive Force

The simplest way to control the speed of a motor is using PWM (Pulse Width Modulation) control. However, the U8 motors have a high back emf. Back EMF (Back Electromotive Force) is the electromotive force that opposes the change in current. BLDC motors have coils inside turning inside magnetic fields and this motion induces the emf known as the back emf. This acts against the applied voltage from the power source and reduces the current applied to the coils. The back emf is proportional to velocity and acts like a damping force. A linear model shown in Eq 3.1 (detailed derivation in Appendix) actively cancels out the back emf by applying positive feedback of the back emf. With a desired torque, proportional to acceleration, and known velocity of the motor, the motor will be able to apply PWM that is needed to keep the torque constant. However,

when this model was applied to the motor, the system behaved nonlinear. This means that there is a hidden state that is not being accounted for the linear model which is the current. Therefore, a nonlinear method is needed to control the motor.

Eq 3.1

$$\text{PWM} = \frac{1}{16}\left(\frac{\ddot{\theta} * R_m * I}{k_t} + k_e * \omega\right)$$

3.2 Force Control Methods

There are three different ways of performing force control on a motor as listed below.

1. Force-feedback method

   Sense torque mechanically using a load cell and implement a PI controller to find the PWM that zeroes the torque error.

2. Current-feedback method

   Sense torque electrically through current and implement a PI control to find the PWM that zeroes the current error.

3. Model-based method

   Sense mechanical states that very torque and use a model to estimate what PWM is needed to generate a desired torque.

For option 1, the load cell will have to be placed on the hopper. However, this is not suitable method because the load cell can potentially break when the hopper hits the ground rendering an impulse of force on the load cell. Option 2 is the most common method of performing torque control. However, the U8 motors do not have the capabilities to sense current. A current

controller can be bought separately and implemented on the hardware. However, that procedure could also cause system integration issues as well as noise. Option 3 does not require any additional sensors but only the encoder that's already available on the motor.

3.3 Experimental Procedure of Model-Based Force Control

The experimental procedure is divided into three sub sections. First, acceleration is experimentally measured across the range of velocity and PWM. Next, Gaussian Process method is used to train the model to construct the three-dimensional lookup table. Finally, the acceleration is calibrated to force using a load cell.

3.3.1 Experimentally Measuring Acceleration Across the Range of Velocity and PWM

From chapter 1 Figure 1.6 (B), the haptic device can be decomposed to two sub blocks: the controller and the motor as shown in Figure 3.1. The model-based controller has two parameters (velocity and force) and estimates the PWM for the motor so that the virtual force will be equal/close to the actual force. For example, to test the hopper's performance in less gravity environment, the virtual force will be set to a positive force. Then the model-based controller will calculate the PWM for the motor to keep that virtual/positive force. The goal is to construct a three-dimensional lookup table of angular acceleration, angular velocity and PWM of the motor. Since angular acceleration is proportional to torque/force, the controller will look up the PWM corresponding to the motor velocity and virtual force (angular acceleration).

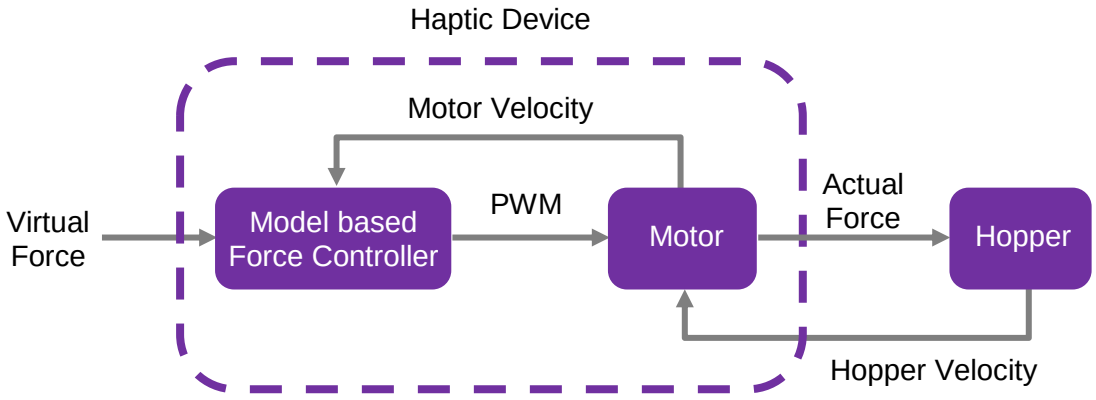

Figure 3.1. Subcomponents of the haptic device block diagram. The haptic device can be decomposed to two parts: controller and the motor. The controller will be performing force control and estimating the PWM needed for the motor to keep virtual force close to the actual force.

A torque speed curve shown in Figure 3.2 exhibits that the velocity and torque increase as the voltage increases. Torque, which is proportional to acceleration, can be found by sweeping the velocity and PWM of the motor. Due to the high torque of the motor, it accelerates to max velocity in 2 ms. Therefore, a flywheel is added to the end of the shaft to increase the inertia of the system and monitor the acceleration as shown in Figure 3.3.

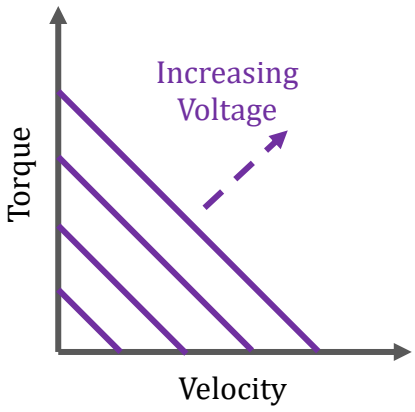

Figure 3.2. Torque-Speed Curve

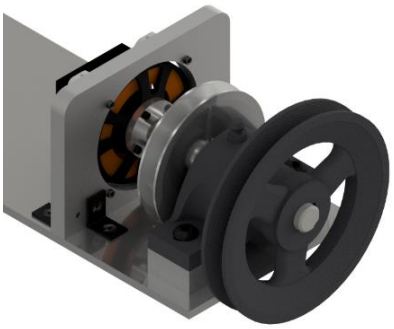

Figure 3.3. CAD model of the flywheel attached

The first experiment is conducted to measure the torque across range of velocity and PWM. With the flywheel attached to the shaft, the motor is excited to a random velocity step input ranging from 0 to 110 rad/s. A PI (Proportional Integral) controller is used for this application. After 500ms, enough time for the velocity to approach steady state, the motor is excited by a random PWM step input ranging from 0 to 1. As shown in Figure 3.4, during the first 500ms, the motor settles to a random velocity of 72.7 rad/s. The motor applies a max PWM to reach to the desired velocity but once it approaches, the PWM settles to just above 0.5. After 500ms, the motor is excited with PWM of 0.4. During that region the velocity is decreasing to the corresponding speed at PWM of 0.4. The goal is to find the slope of velocity during constant PWM in which the velocity is linearly increasing/decreasing.

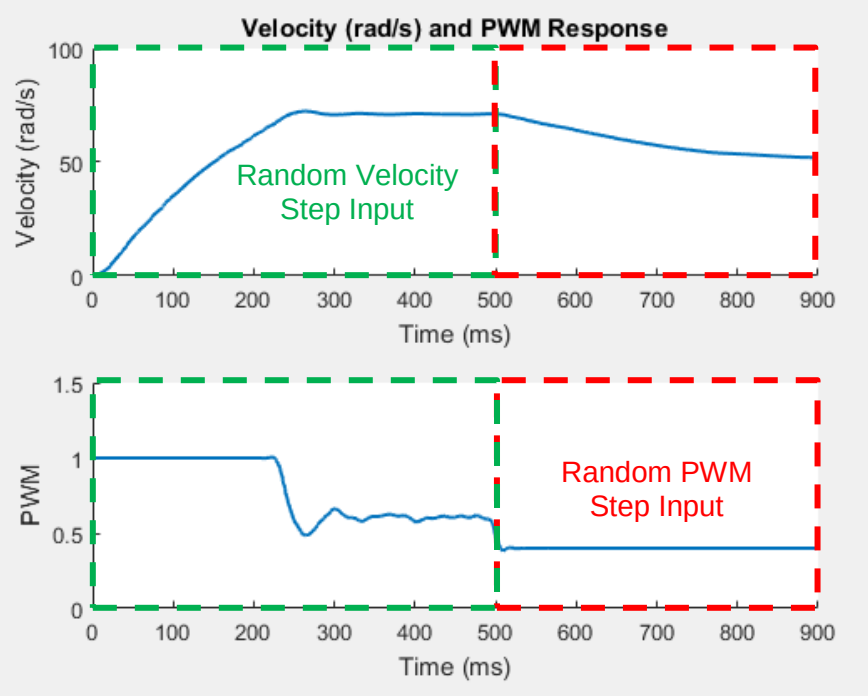

Figure 3.4. Motor running a random velocity step input for the first 500ms then a random PWM step input after 500ms

Figure 3.5 is one of the zoomed in trials of Figure 3.4 Velocity (rad/s) vs. Time(m/s) plot. (A) shows the region where the motor is exited with a random -0.16801 PWM after the motor reaches a random steady state velocity of 66.0838 rad/s. (B) shows the zoomed in portion (purple box) of (A). Next, linear regression is used on a window size of 10ms (+/- 5ms about 535ms) to find acceleration. The average velocity is found by taking the mean. So, for each trial, one acceleration value will be found for one PWM and one velocity value. Figure 3.6 shows another trial where the velocity is increasing due to a high random PWM. A total of 2077 trials were conducted to sweep the PWM and velocity space and the motor update rate is set at 1k Hz and the data is also sampled at 1k Hz.

(A)

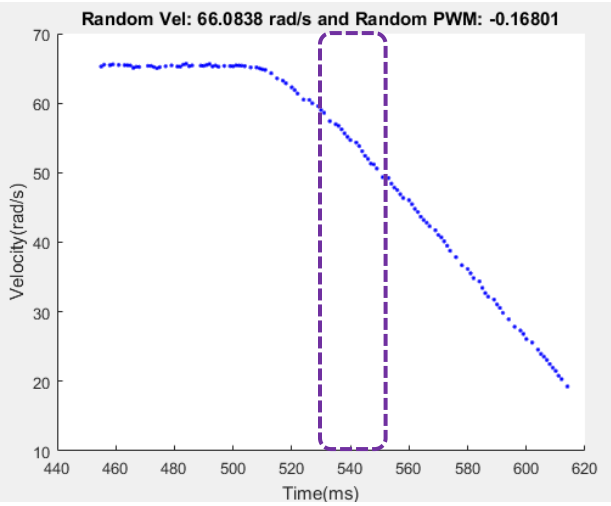

(B)

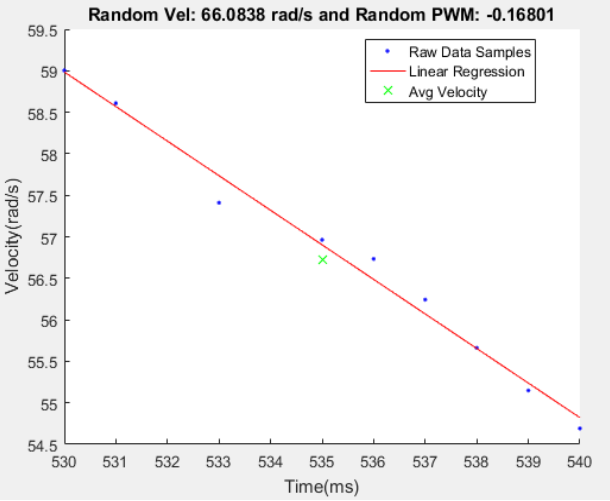

Figure 3.5. Region where the motor is excited with a random -0.16801 PWM after it reaches a random steady state 66.0838 rad/s velocity (A). Zoomed in region of (A) of 10ms window size. Linear regression used to find the slope for this region that has a constant PWM (B).

(A)

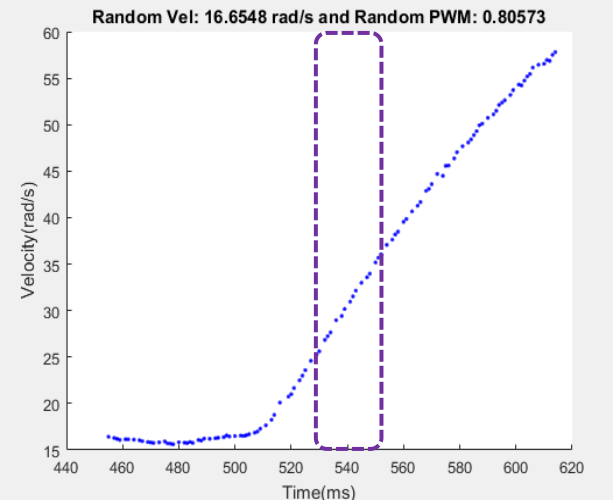

(B)

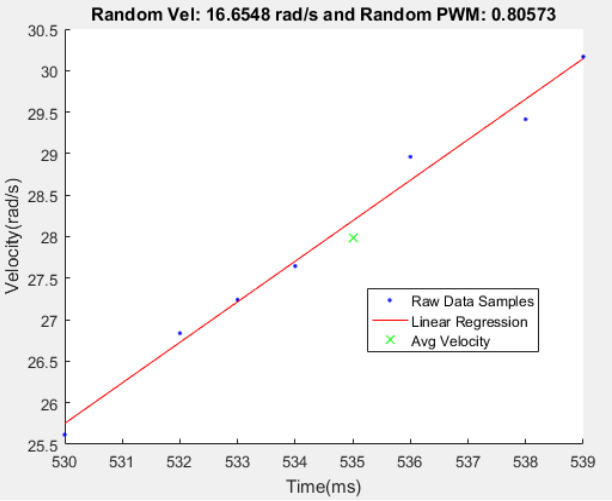

Figure 3.6. Another trial similar to that of Figure 3.5. The motor settles to the desired random velocity of 16.6548 rad/s but then increases due to the high random PWM value of 0.80573 (A). Zoomed in region of (A) in which the window size is 10 ms. Linear regression used to find the slope for this region that has a constant PWM (B).

The region to implement linear regression (B) cannot be right after 500ms since the decay of velocity is non-linear around 500ms due to impedance of the current as shown in Figure 3.5 (A). Therefore, the region cannot be too close to 500ms but also not too far from 500ms because choosing the region too far from 500ms will bias the velocity data. In other words, there'll be less high velocity data around max velocity since the average of the velocity measurements will be much lower than the random velocity.

3.3.2. Using Gaussian Process to Train the Model

Figure 3.7 (A) shows the 2077 trials of the PWM and velocity pairs. This shows the unbiased data spread throughout the velocity and PWM space. Each of the 2077 PWM and velocity pairs also have 2077 acceleration data associated to it. The red dots on (B) are the data plotted in the three-dimensional space (PWM vs. Acceleration (rad/s^2) vs. Velocity (rad/s)).

Gaussian Process is used to train the model and construct a surface. Gaussian process produces a smooth function and is simple to implement for a nonlinear function approximation. Just visually, the surface shows that the system is acting nonlinear since the surface is not a plane.

(A) (B)

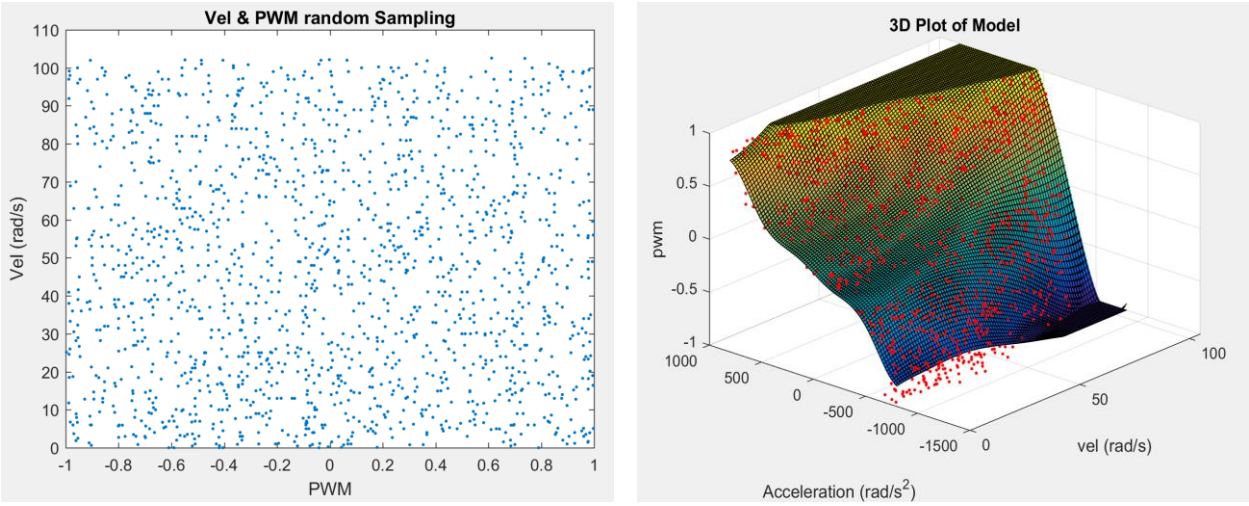

Figure 3.7. 2077 trials of PWM and Velocity pairs sampled in the PWM-Velocity space (A). A surface of the PWM vs. Acceleration (rad/s^2) vs. Velocity (rad/s) found using Gaussian Process.

Figure 3.8 is the contour plot of the surface found above Figure 3.7 (B). The contour plot of (A) is similar to the torque-speed curve from Figure 3.2. However, the plot also exhibits the non-linearity in the system. The contour plot also depends highly on the region and the window size where the linear regression is used to find the acceleration in the previous step. Although the same region and window size is used to find the acceleration for the velocity spectrum, adjusting the region and window size differently for lower and higher velocity can change the contour plot. When the virtual force is set (e.g. acceleration = 105.1 rad/s^2), the motor will follow the PWM path shown in (B) to keep the constant force.

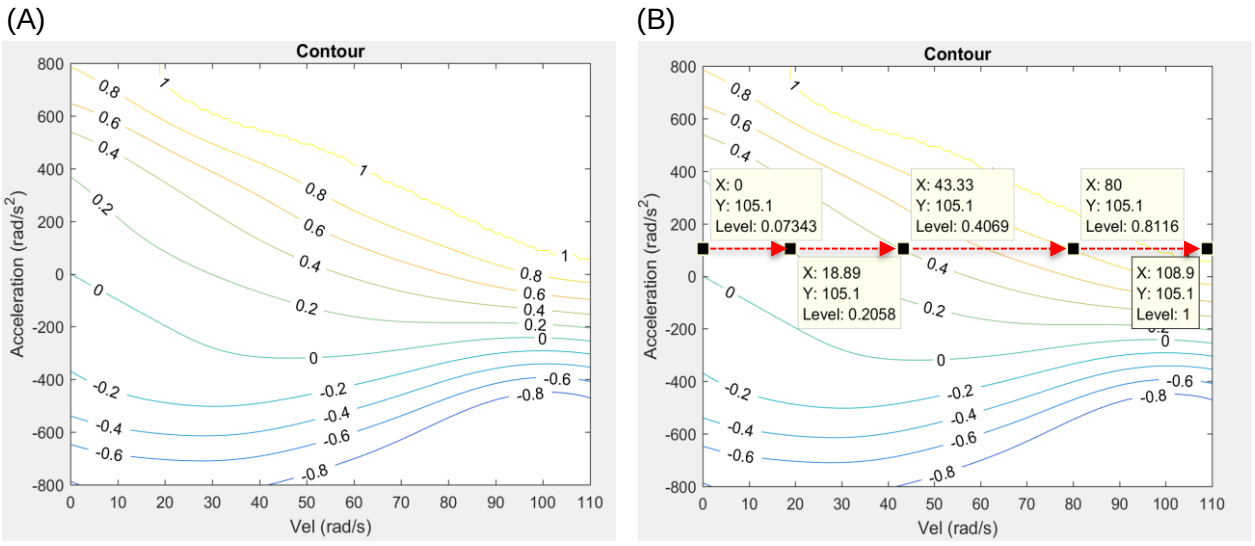

Figure 3.8. Contour plot of the surface found using Gaussian Process (A). PWM path that the motor will follow when applying a constant acceleration of 105.1 rad/s^2.

3.3.3. Calibrating Acceleration to Force using a Load Cell

The last step is to calibrate the acceleration to force. First, the load cell is integrated with the mainboard. Figure 3.9 shows how the LCM 100 signal is sent to the mainboard. For this procedure, LCM 100 load cell and IAA 100 amplifier from FUTEK were used. LCM 100 is connected to IAA 100 Amplifier which amplifies the voltage signal to +/- 5V. However, the mainboard for the motors has a range of 0 to 3.3V. Therefore, a simple circuit board was designed to rectify the signal and convert the range to 3.3V.

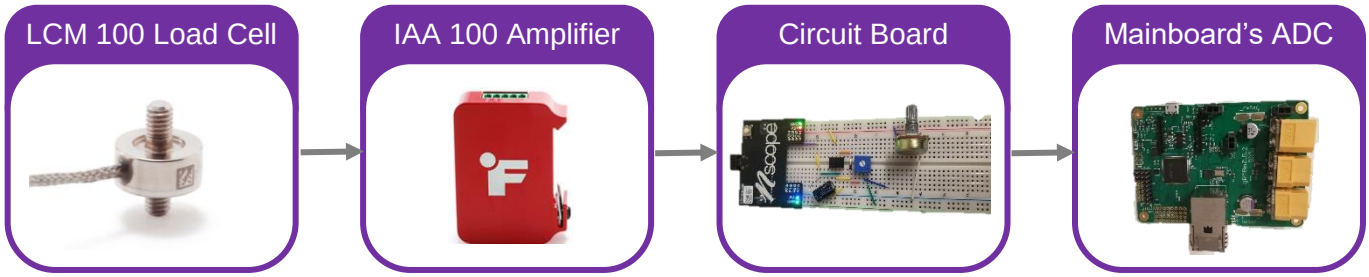

Figure 3.9. Schematic diagram of the LCM 100 connection to the mainboard

The circuit board is composed of a capacitor, op-amp, voltage divider and a diode. A nScope (portable oscilloscope) and a potentiometer are used to verify the output of the circuit. Figure 3.10 shows the input and output signal; each division is 2 V. The input signal (+/- 5V) is provided by the potentiometer and the output signal is measured at the end of the circuit. The yellow signal is the input signal and the red signal is the output signal. The output signal is rectified when the input voltage is negative and $\text{output signal} = \frac{3.3}{5} * \text{input signal}$.

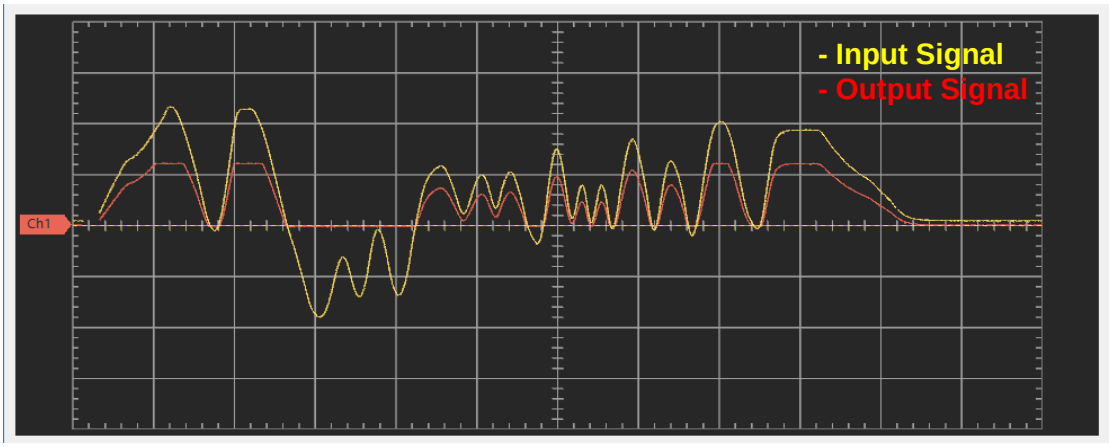

Figure 3.10. Input signal (-5 to +5V) and the output signal (0 to 3.3V) after the signal goes through the circuit board.

The load cell is placed right above the top plate with static load for different acceleration. Figure 3.11 shows the load cell reading for acceleration of 56 rad/s^2 and 347 rad/s^2. Low pass filter is used to filter the noise.

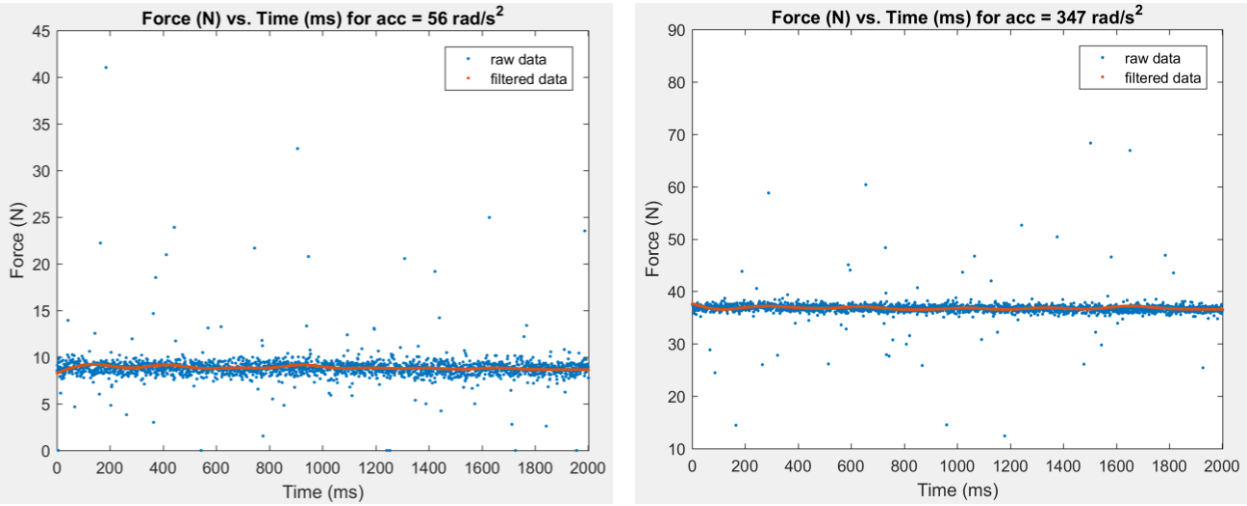

Figure 3.11. Load cell used to calibrate acceleration (rad/s^2) to force (N)

Seven different pair of acceleration and force data are collected to find the linear relationship between linear force and angular acceleration. The result yielded $F = 0.0934\dot{\omega} + 5.2003$ with $R^2 = 0.9876$.

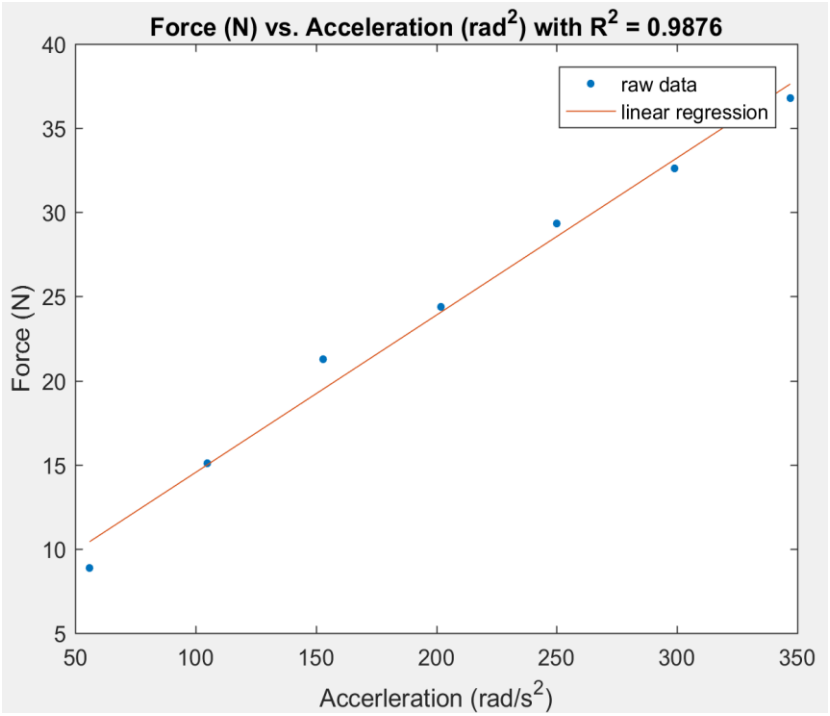

Figure 3.12 Linear relationship between acceleration (rad/s^2) to force (N)

3.4 Summary

This chapter focused on the experimental procedure of implementing a model-based force control on the haptic device. Due to the nonlinearity of the system, a 3D lookup table is used to construct a surface. Finally, the load cell is integrated into the system to calibrate the acceleration to force. In short, force control can be implemented into the system to perform the tests.

Chapter 4

Haptic Device Characterization

This chapter focuses on characterizing the haptic device's performance; quantifying how well the force control is performing the for the haptic system by finding the force errors over the range of frequencies the hopper resides. If the haptic device is applying zero net force to the hopper, it should perform the same with/without the haptic device.

4.1 Hopper Frequency

To characterize the haptic system, it is important to first find the frequency at which the hopper predominantly resides. The reflective maker is attached on the body (front side) of the hopper with a motion capturing camera placed 2 m from the hopper. The camera's sampling frequency is set to 1k Hz and the haptic device is not attached. Figure 4.1 (A) shows the hopper's position data. After differentiating the position data and applying FFT, the frequency at which the hopper resides can be found as shown in (B). The hopper's dominant frequency is 2.3Hz. The other spikes in the plot are the resonant frequencies.

(A)

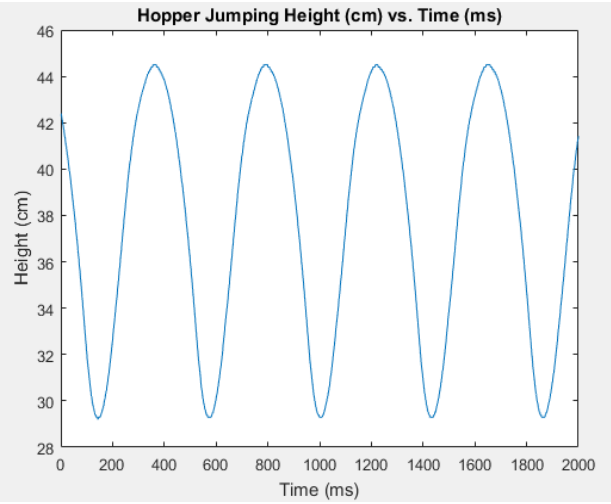

(B)

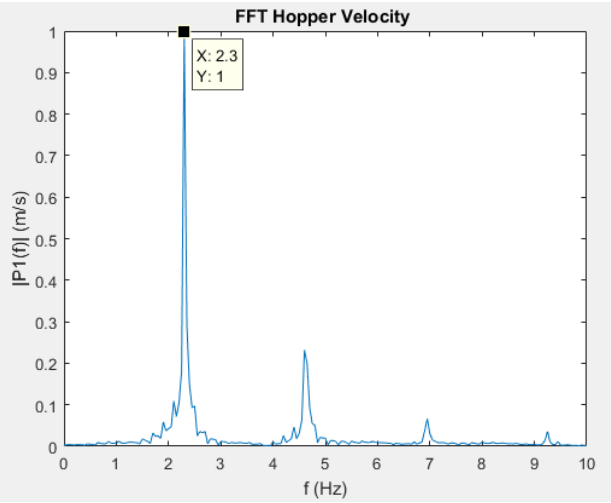

Figure 4.1. Hopper's position (height) collected using a motion capturing camera (A) The frequency of Hopper's velocity found applying FFT on velocity data (B). Hopper's dominant frequency is 2.4 Hz.

4.2 Experimental Procedure of Haptic Device Characterization

The goal for this experiment is to quantify how well the force control is working on the haptic device. This can be resolved by finding the transfer function that outputs the magnitude of force error the haptic system will apply to the robot in response to velocity signals at different frequencies.

First, the experimental setup is explained. The top and bottom are connected with a load cell in the middle. Second, the sum of sines trajectory is explained and why that method is chosen for the bottom motor. Furthermore, FFT is applied on the input and output signal to find the transfer function. Last, the transfer function is used on the velocity input FFT signal to find the force error. If the model for the force control on the top motor is perfect, the load cell should read a constant force regardless of the position control on the bottom motor.

4.2.1 Experimental Setup

For this experiment, the top and bottom are connected with a load cell in the middle. The load cell is attached to the top plate which is constrained to 1 DOF. The carriage is used to prevent any horizontal deflection of the load cell. The top motor is connected to the top of the load cell and a spring is added between the bottom plate and bottom motor. The spring is added to prevent the cable coming off the pullies in case slack occurs in the cable. Also, it reduces the transient load from the load cell which can damage the load cell. Figure 4.2 (A) is the schematic diagram of the setup and (B) is the actual hardware setup.

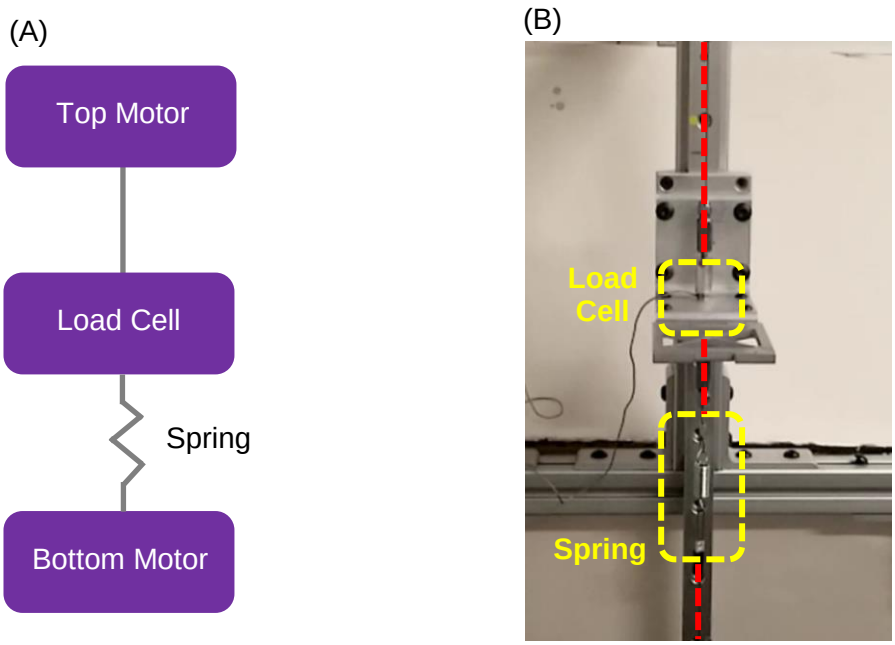

Figure 4.2. Schematic diagram of the setup (A) Actual setup (B)

4.2.2 Sum of Sines and FFT

For this experiment, the top motor will be used as the haptic device and the bottom motor as the user. Therefore, the top motor will be commanding force control that was found in chapter 3 and the bottom motor will be commanding a sum of sines position trajectory. Although the bottom motor is commanding position control (Eq 4.1), the velocity of the top motor will be used for the input velocity (Eq 4.2). This is because the top motor is used as the haptic device. Figure 4.3 shows the velocity of the top and bottom motor when force control and sum of sines position control are commanded to the top and bottom motor respectively. Despite the load cell, spring and cable attachment between the two motors, the top motor's velocity matches closely to that of the bottom motor. This ensures that the system can be considered as one rigid system.

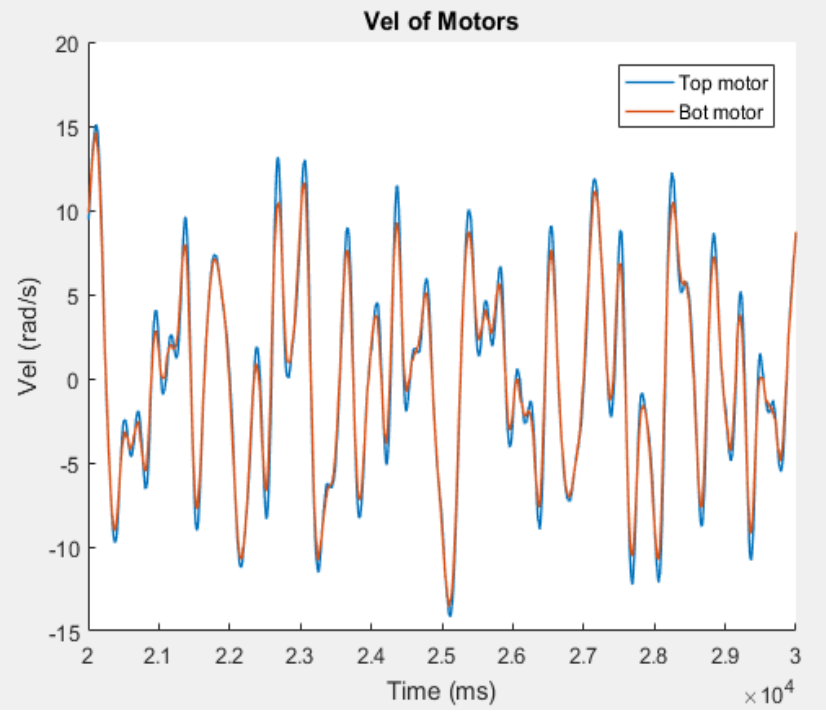

Figure 4.3. Velocity of the top and bottom motor from motor encoder

The sum of sines trajectory (Eq 4.3) is seven distinct sine waves (Eq 4.2) with different frequencies and amplitude. The phase for each sine waves are randomized so that the summation of seven distinct sine waves will generate different trajectory. Figure 4.4 (A) and (B) shows two different velocity trajectories because the phase is randomized every experiment. Since the hopper's dominant frequency is at 2.3Hz, the frequencies chosen for characterizing the performance of the hopper are 0.7, 1.1, 1.7, 2.3, 3.1, 4.1, 4.7 Hz. These are prime numbers divided by 10 and the amplitude is 1/(1.5*frequency). Since the amplitude decreases as frequency increases, the product of the amplitude and frequency is constant for all seven distinct sine waves. This method is chosen because it is tougher for the motors to track at a high frequency with high amplitude due to motor inertia. Also, due to the constraint of the length of the linear guide rail, the sum of amplitude has to be within 25 cm.

$$y(t) = Asin(wt + \varphi) \quad \text{Eq 4.1}$$

$$\dot{y}(t) = A\omega cos(wt + \varphi) \quad \text{Eq 4.2}$$

$$Y_i(t) = \sum y_i(t) = \sum_{i=1}^{7} A_i \sin(2\pi f_i t + \varphi_i) \quad \text{Eq 4.3}$$

(A)

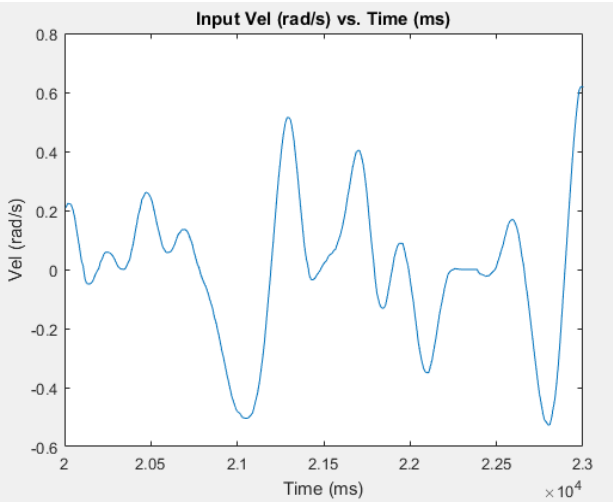

(B)

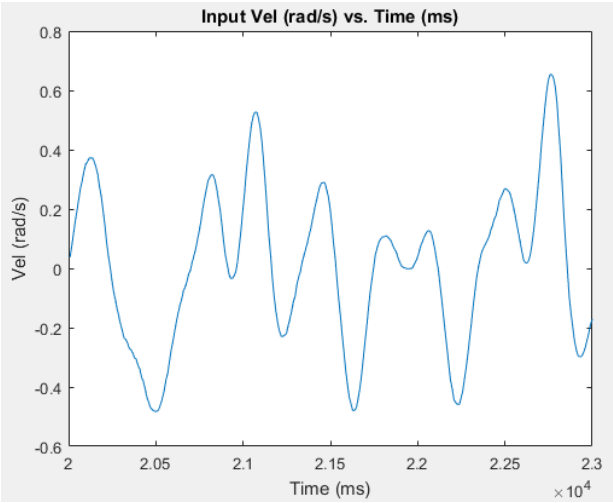

Figure 4.4. Two different velocity trajectories due to randomized phase

When applied FFT (Fast Fourier Transform) to a signal in the time domain, the signal is decomposed to single sinusoidal oscillations at distinct frequencies with distinct amplitude and phase; the signal is converted from the time domain to frequency domain. Since the input signal is commanded with known frequencies, the output signal from the load cell should be dominant at those frequencies.

Figure 4.5 (A) shows the velocity signal in the time domain from the top motor. The signal is directly achieved from the encoders from the motor. (B) shows the FFT of the (A) signal. The frequencies where the power is visibly higher matches the selected frequencies for the sum of sines trajectory. As mentioned earlier, the input magnitude for the desired frequencies should be the same since the amplitude and frequency are inversely proportional. However, (B) illustrates that the magnitude rolls off as the frequency rises. This is because the motor inertia and motor dynamics of the bottom motor acting like a low-pas filter.

(A)

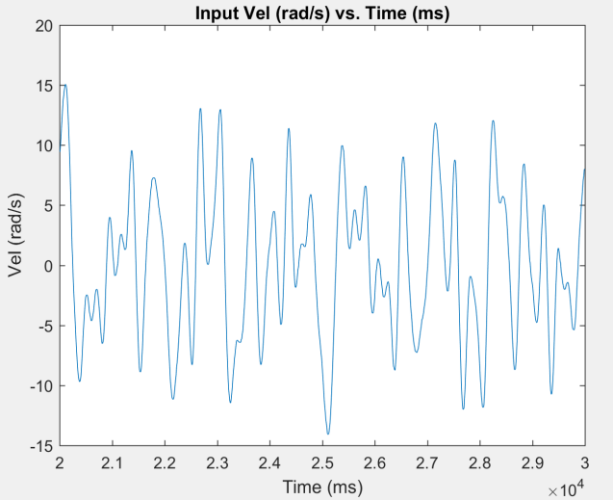

(B)

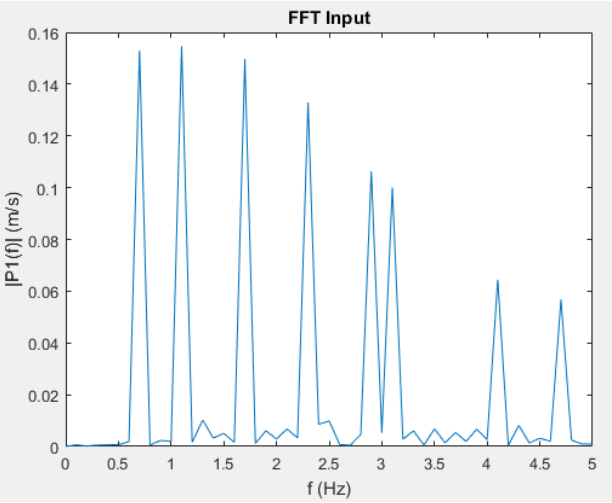

Figure 4.5. Input velocity signal from the top motor (A). FFT of the input signal (B)

Similarly, Figure 4.6 (A) shows the force signal in the time domain from the load cell. (B) shows the FFT of the (A) signal. Once again, the frequencies where the power is visibly higher matches the selected frequencies for the sum of sines trajectory.

(A) (B)

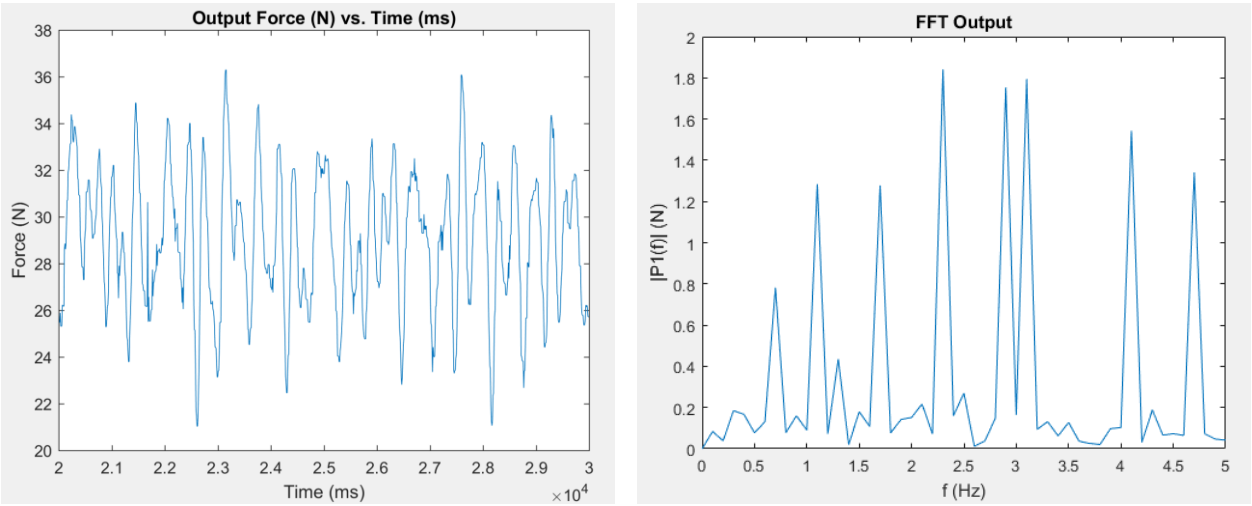

Figure 4.6. Output force signal from the load cell (A). FFT of the output signal (B)

4.2.3 Finding Transfer Function and Estimating the Force Error

By sweeping the range of frequencies that the hopper resides, the transfer function will yield the magnitude of the force error the haptic system will apply to the hopper in response to velocity signals at different frequencies. Ten trials are conducted to find a transfer function (Eq 4.4) for the frequencies of interest. The 'x' marks on Figure 4.7 are the individual transfer function for each desired frequency. And the 'O' marks are the mean of the ten trials for each frequency. Figure 4.7 shows that the transfer gain increases as the frequency increases. This confirms that the haptic device does worse force tracking at higher frequency. If the system were linear and the force tracking were perfect, the 'x' marks will overlap to one point and the trend will be horizontal as frequency increases.

$$TF = \frac{|Force(freq)|}{|Vel(freq)|} \qquad \text{Eq 4.4}$$

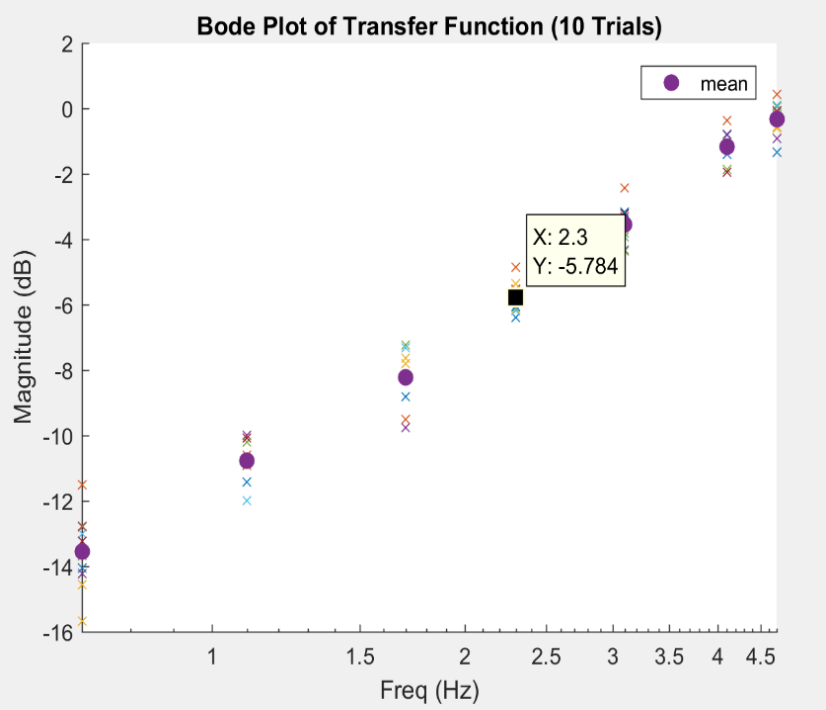

Figure 4.7. Bode plot of the transfer function

Once the gains for transfer function are found at the desired frequencies, all the unknown gains between the desired frequencies are linearly interpolated. Finally, once all the gains are found for the frequency range between 0.7 and 4.7 Hz, the gains are multiplied to the hopper's velocity FFT plot. Figure 4.8 (A) shows the hopper's velocity bode plot and (B) shows the estimated force bode plot for the frequency range between 0.7 and 4.7 Hz. This result shows that haptic device will apply about 13N (half the body weight) of force error to the hopper operating at 2.3Hz.

(A) (B)

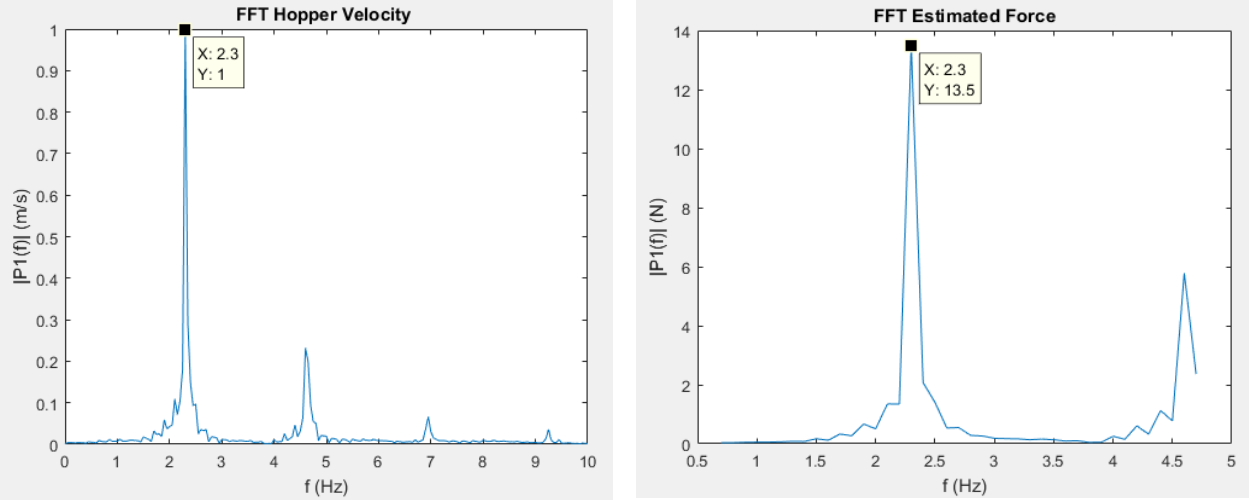

Figure 4.8. FFT of the hopper velocity (A) 13.5N force error at 2.3 Hz (B)

4.3 Results and Discussion

Figure 4.7 illustrates that the system is acting close to a high pass filter; the signal attenuates at low frequencies. The gain at higher frequency is almost 0 dB whereas the gains at lower frequency are negative. In an ideal scenario, the bode plot trend should look horizontal at negative gain since the magnitude of the input is constant and the magnitude of the output is 0. In short, Figure 4.8 shows that the haptic device does work at low frequencies. But the performance is worse at higher frequency. There are couple reasons why the body plot is does not look horizontal.

- The experimental procedure when collecting the input and force data to construct the bode plot does not put into account any impacts that the hopper experiences.
- The input signal is not constant. And this was already verified from Figure 4.5 (B).
- The inertia of the system and the noise of the system (e.g. encoder, ADC, load cell).
- The bottom motor behaves differently to the top motor, so the model found for the top motor is not an accurate for the bottom motor.

Chapter 5

Testing the Haptic System with Hopper

This chapter closes the loop with the hopper in the loop. The hopper has two states: contraction and extension. The hopper is dropped 20cm above ground while its initial state is in contraction. The velocities of the motors are monitored and when velocities of the two motors changes due to the impact, the motors on the hopper commands extension mode in which PWM of 0.8 is powered. The extension allows the hopper to push off from the ground. When the legs approach to a certain position during extension, the mode is switched back to contraction during the ballistic phase. The process is repeated allowing a smooth jumping motion from the hopper.

With the hopper in the loop, two experiments are tested. First, a zero-net force of equal but opposite forces are commanded by the two haptic devices. Then, a positive net force is commanded by the two haptic devices. A motion capturing camera is used to capture the hopper's dynamics at 1k Hz.

5.1 Zero Net Force Experiment

To test the haptic device with the hopper in the loop, the haptic devices are applying equal but opposite forces on to the hopper so that the net force on the hopper is zero. If the haptic device is perfectly designed, the hopper's jumping height should be equal with or without the cable since there's zero force on the hopper. In other words, the hopper should be experiencing the same environment with or without the cable. Figure 5.1 (A) shows a free body diagram of the setup. Figure 5.1 (B) yields that the haptic device is not truly applying a net force of 0N since the hopper is jumping less high with the haptic device attached. Without the cable, the hopper can jump up to 32cm but with the cable it jumps up to 25cm.

This result supports the findings from Chapter 4 Section 4.2.3. The characterization of the haptic device yielded that the it will have an error of 13N. This again shows the importance of designing the haptic system to cancel out the inertia of the system. Due to the mass of the inertia added to the hopper, it cannot jump as high. Actively cancelling the inertia of the system, or reducing the mass of the haptic device parts, will reduce the error of the transfer function bode plot. The key for this test is for the haptic device to have minimal influence on hopper's dynamics.

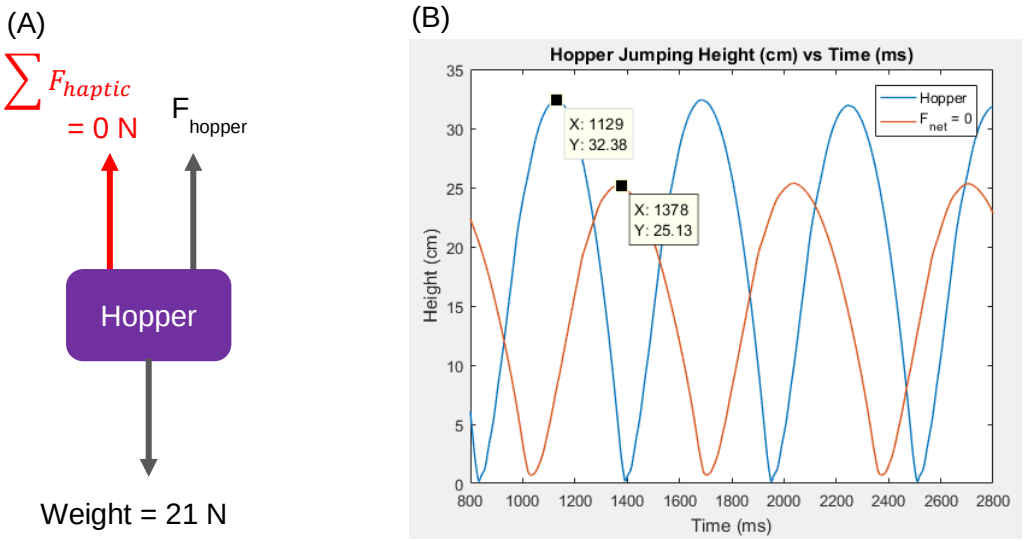

Figure 5.1. Free body diagram of the hopper (A) Hopper height trajectory at zero net force (B)

5.2 Positive Net Force Experiment

The second experiment involves the haptic device commanding a positive net force on the hopper. For this experiment, the bottom motor is applying 15N and the top motor is applying 28N. Since the weight of the hopper is reduced to 8N, it experiences 0.38g of gravity. Figure 5.2 (A) shows the free body diagram of the setup and (B) shows the trajectory found from the motion capturing camera. It shows that the hopper jumps 4-5cm higher with lower frequency which shows that the hopper is operating in less gravity environment.

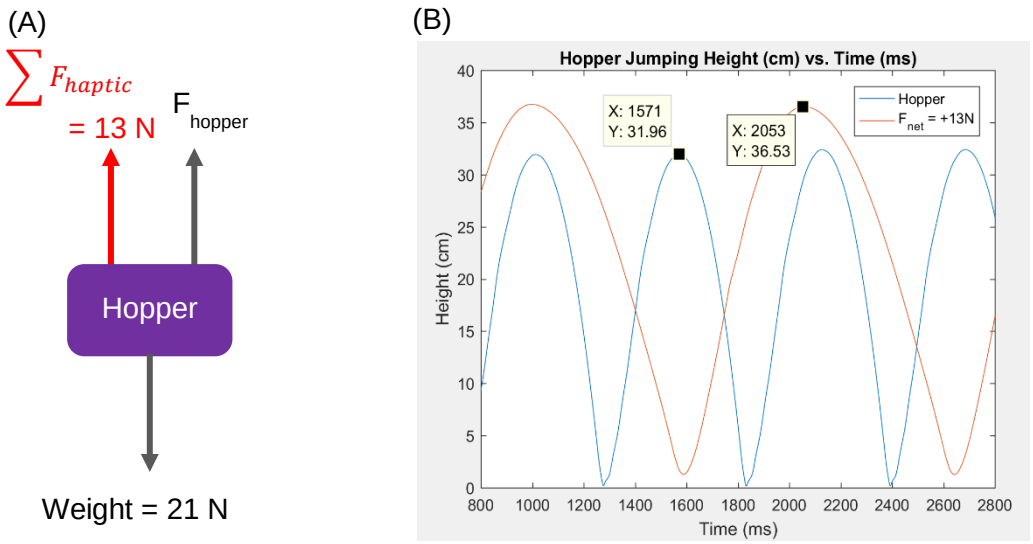

Figure 5.2. Free body diagram of the hopper (A) Hopper height trajectory at positive net force (B)

5.3 Summary

This section empirically tested the haptic device with the hopper in the loop. The motor characterization verifed the jumping height error that occurred when applied zero net force. This is suspected to be mainly due to the added mass from the haptic device. This can be resolved by actively feedforward cancelling the inertia of the system [2] or redesigning the haptic module with less mass. However, the positive net force showed that the haptic device could render forces to emulate less gravity environment for the robot.

Chapter 6

Conclusion and Future Work

This section summarizes all the preceding chapters and mentions what can be done to improve the current work.

6.1 Conclusion

Chapter 1 focuses on the overarching high-level goal as well as introducing the haptics field. The goal for this research is to design a testbed that can render virtual dynamics to emulate different environments and perturb it in a systematic/repeatable method. The motivation for this research originated from the need for testing/perturbing robots in a systematic method and the need for testing robots in different environments. A novel perspective of haptics is introduced; a robot interacting with a testbed and experiencing virtual environment is analogues to human interacting with a haptic device.

Chapter 2 mainly focuses on the mechanical design of the testbed and why certain design methods were chosen. By using one of the legs of the Minitaur, a testbed was designed, prototyped, and manufactured using cable mechanism which was inspired by a cable-driven parallel robot.

Next, Chapter 3 illustrates the experimental procedures to achieve force control on the motor using model-based force control. Acceleration is experimentally measured by sweeping the range of velocity and PWM. Next, Gaussian Process is used to train the model and a load cell is used to calibrate the acceleration to force. Using this model-based force control, the motors are able to apply constant forces through this nonlinear lookup table method.

Chapter 4 also concentrates on the experimental procedure in characterizing the motor performance. A unique sum of sines method is implemented to generate the trajectory for the bottom motor. Then FFT is applied to the input and output of the signal to find the transfer function. Ultimately the gain is multiplied to the FFT input signal of the hopper's velocity to find the magnitude error of the force. The result yields that the magnitude of force error the haptic system applies to the user/hopper is around 13N.

Finally, chapter 5 closes the loop by adding the hopper to the haptic system. As the motor characterization results show, the hopper does not jump the same amount with the cable attachment. This is mainly due to the added mass from the haptic device. However, with a positive net force, the hopper is able to jump 5 cm higher with lower frequency which demonstrate the hopper experiencing less gravity. Overall, a haptic system is successfully built in which it can render virtual dynamics to the hopper and alter the environment that the hopper is operating.

6.2 Future Work

There are couple things that can be implemented to enhance the haptic system. First, for this haptic device to be a true impedance haptic device, the inertia of the system must be close to zero. This can be achieved by actively cancelling the inertia of the system by a feedforward method [2] or by mechanically redesigning the parts to reduce the mass. One method of reducing the inertia is to print out a pulley using a 3D printer and using a lighter, thinner shaft. Moreover, a smaller ball bearing to support the opposite end of the motor will reduce friction. The results from Chapter 5 shows that the hopper experiences an added mass of the haptic system when connected. By reducing the inertia, the haptic device will be able to render more accurate bode plot for the transfer function. Second, tuning the controller will enhance the performance. The model for the top motor is implemented on the bottom motor with an assumption that the two motors are the same. However, the motors can be different as well as the parts that are attached to the motors. A careful screening of the controllers, mechanical designs, and digital signal processing will enhance the performance.

6.3 Future Question

Most of the haptic devices are limited in that the users can only interact with the haptic device through a continuous and slow trajectory. However, for this research, the user (hopper) is dynamically contact rich with discontinuities at impact. It will be interesting to see if the haptic device can predict the collision and provide less tension during the impact. A haptic system designed for a rapid changing dynamical system will open a new field in haptics.

Appendix

$$V_m = V_s - V_b$$

$$I_m * R_m = (16 * PWM) - (k_e * \omega)$$

$$I_m = \frac{(16 * PWM) - (K_e * \omega)}{R_m}$$

$$I_m = \frac{\tau}{k_t}$$

$$\tau = \frac{(16 * PWM) - (K_e * \omega)}{R_m} * k_t$$

$$\tau = I\ddot{\theta}$$

$$\ddot{\theta} = \frac{(16 * PWM) - (K_e * \omega)}{R_m * I} * k_t$$

$$\text{PWM} = \frac{1}{16}\left(\frac{\ddot{\theta} * R_m * I}{k_t} + k_e * \omega\right)$$

V_m : Motor voltage
V_s : Source voltage
V_b : Back-EMF
I_m : Current through the motor
R_m : Resistance through the motor
k_e : Motor constant
k_t : Motor constant
I : Moment of inertia

Appendix 1. Full testbed setup

Appendix 2. Hopper setup

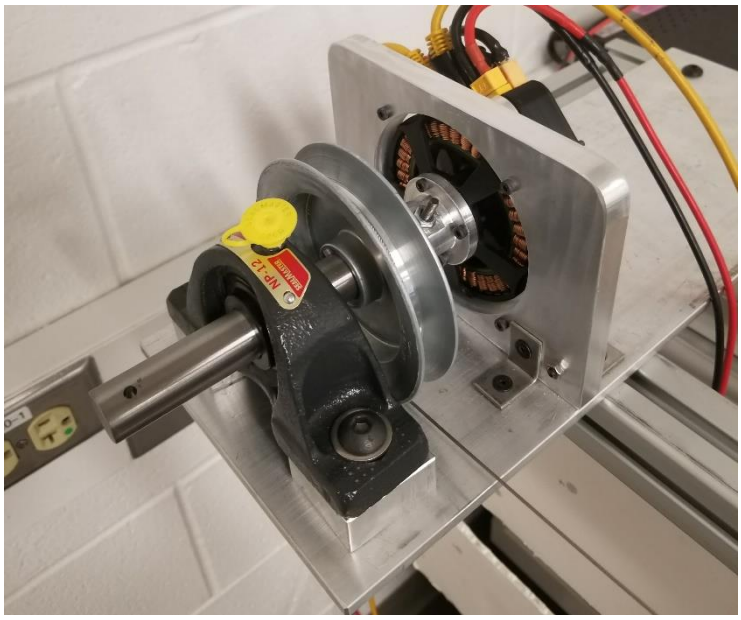

Appendix 3. Haptic device setup

Bibliography

[1] Hannaford B., Okamura A.M. (2008) Haptics. In: Siciliano B., Khatib O. (eds) Springer Handbook of Robotics. Springer, Berlin, Heidelberg

[2] J. Gil, A. Rubio, and J. Savall, “Decreasing the Apparent Inertia of an Impedance Haptic Device by Using Force Feedforward,” IEEE Transactions on Control Systems Technology, vol. 17, no. 4, pp. 833–838, 2009.

[3] Du, Jingli, and Sunil K. Agrawal. “Dynamic Modeling of Cable-Driven Parallel Manipulators with Distributed Mass Flexible Cables.” Journal of Vibration and Acoustics, American Society of Mechanical Engineers, 1 Apr. 2015

[4] F Qian, DI Goldman - Robotics: Science and Systems, 2015. “The dynamics of legged locomotion in heterogeneous terrain: universality in scattering and sensitivity to initial conditions.”

[5] Wen, K., et al. “HAPTIC FORCE CONTROL BASED ON IMPEDANCE/ADMITTANCE CONTROL.” Egyptian Journal of Medical Human Genetics, Elsevier, 2 May 2016

[6] J. Baldassini. An Examination of the Effects of Deformable Foam Contact Surfaces on Robotics Locomotion. University of Washington, Seattle, WA, USA, 2017.

[7] Y. Sosnovskaya. External Measurement System for Robot Dynamics. University of Washington, Seattle, WA, USA, 2017

[8] Morris, Melissa & Shoham, Moshe. (2009). Applications and Theoretical Issues of Cable-Driven Robots.

[9] Samur, Fei Wang, Spaelter, & Bleuler. (2007). Generic and systematic evaluation of haptic interfaces based on testbeds. Intelligent Robots and Systems, 2007. IROS 2007. IEEE/RSJ International Conference on, 2113-2119.

[10] Kenneally, G., & Koditschek, D. (2015). Leg design for energy management in an electromechanical robot. IEEE International Conference on Intelligent Robots and Systems, 2015, 5712-5718.

[11] Mason, Matthew T. ”Compliance and force control for computer controlled manipulators.” Systems, Man and Cybernetics, IEEE Transactions on 11.6 (1981): 418-432.

[12] McMahan, William, and Katherine J. Kuchenbecker. ”Haptic display of realistic tool contact via dynamically compensated control of a dedicated actuator.” Intelligent Robots and Systems, 2009. IROS 2009. IEEE/RSJ International Conference on. IEEE, 2009.

[13] C. R. Carignan and K. R. Cleary., Closed-loop force control for haptic simulation of virtual environments Haptics-e [Online], vol (2). Available: http://www.haptics-e.org

[14] Ham, R. V., et al. ”Compliant actuator designs.” Robotics & Automation Magazine, IEEE 16.3 (2009): 81-94.
[15] Seok, Sangok, et al. ”Actuator design for high force proprioceptive control in fast legged locomotion.” Intelligent Robots and Systems (IROS), 2012 IEEE/RSJ International Conference on. IEEE, 2012.
[16] Raibert, Marc H., and John J. Craig. ”Hybrid position/force control of manipulators.” Journal of Dynamic Systems, Measurement, and Control 103.2 (1981): 126-133.
[17] Hogan, Neville. ”Impedance control: An approach to manipulation: Part IIImplementation.” Journal of dynamic systems, measurement, and control 107.1 (1985): 8-16.
[18] Qian, F. I., & Goldman, D. (2015). The dynamics of legged locomotion in heterogeneous terrain: Universality in scattering and sensitivity to initial conditions. Robotics: Science and Systems, 11, .
[19] Jeffrey Aguilar, & Daniel I. Goldman. (2015). Robophysical study of jumping dynamics on granular media. Nature Physics, 12(3), 278-283.
[20] Revzen, S., Burden, S., Moore, A., Mongeau, T., & Full, Y. (2013). Instantaneous kinematic phase reflects neuromechanical response to lateral perturbations of running cockroaches. Biological Cybernetics,107(2), 179-200.
[21] Hubicki, C., Aguilar, J., Goldman, D., & Ames, A. (2016). Tractable terrain-aware motion planning on granular media: An impulsive jumping study. Intelligent Robots and Systems (IROS), 2016 IEEE/RSJ International Conference on,2016, 3887-3892.
[22] Donelan, Shipman, Kram, & Kuo. (2004). Mechanical and metabolic requirements for active lateral stabilization in human walking. Journal of Biomechanics, 37(6), 827-835.